Title: Mapping Permafrost Variability and Degradation Using Seismic Surface Waves, Electrical Resistivity and Temperature Sensing: A Case Study in Arctic Alaska

Authors: Ahmad Tourei[1], Xiaohang Ji[2], Gabriel Fernando Rocha dos Santos[3], Rafal Czarny[3], Sergei Rybakov[4], Ziyi Wang[2], Matthew Hallissey[2], Eileen R. Martin[1,5], Ming Xiao[2], Tieyuan Zhu[3], Dmitry Nicolsky[4,6], Anne Jensen[7]

[1] Hydrologic Science and Engineering Program, Colorado School of Mines, Golden, CO, USA, [2] Department of Civil and Environmental Engineering, The Pennsylvania State University, University Park, PA, USA, [3] Department of Geosciences, The Pennsylvania State University, University Park, PA, USA, [4] Geophysical Institute, University of Alaska Fairbanks, Fairbanks, AK, [5] Department of Geophysics and Department of Applied Math and Statistics, Colorado School of Mines, Golden, CO, USA, [6] Laboratory for Integrated Research of the Arctic Land-Shelf System, Tomsk State University, Tomsk, Russia,[7] Department of Anthropology, University of Alaska Fairbanks, Fairbanks, AK, USA.

Corresponding author: Ahmad Tourei (tourei@mines.edu)

This paper is a non-peer reviewed preprint submitted to Earth ArXiv.
This paper has been submitted to the Journal of Geophysical Research: Earth Surface for publication consideration.

Abstract

Subsurface processes are a driving factor behind some surface processes in permafrost regions, but multiple geophysical techniques are needed to reliably constrain the strength, water saturation, and ice content of permafrost across these heterogeneous regions. This research investigates the spatial variability of permafrost in undisturbed tundra and the permafrost degradation in disturbed tundra in Utqiaġvik, Alaska, using multiple geophysical techniques. Here, we integrate multichannel analysis of surface waves (MASW), electrical resistivity tomography (ERT), and ground temperature sensing to examine heterogeneity in permafrost's geophysical characteristics. Using MASW, we find that the active layer's shear wave velocity, V_s, ranges from 240 to 370 m/s, and the permafrost's V_s ranges from 450 to 1700 m/s. These V_s profiles reveal cryostructures such as cryopeg and ice-rich zones in the permafrost layer. Additionally, we find an inverse relationship between in-situ V_s and ground temperature measurements. The integrated results of MASW and ERT provide valuable information for verifying ERT results for characterizing permafrost heterogeneity and cryostructure. This combination of geophysical and temperature sensing methods provides a new, robust approach to assess the spatial variability of permafrost in a coastal environment. Our results also indicate that civil infrastructure systems such as gravel roads and pile foundations affect permafrost by thickening the active layer, lowering the V_s, and reducing heterogeneity. Then, we show how the resulting V_s profiles can be used to estimate key parameters for designing buildings in permafrost regions and maintaining existing infrastructure in polar regions.

Plain Language Summary

This study examines permafrost variability across a range of disturbed and undisturbed locations in Utqiaġvik, Alaska, using a variety of geophysical and temperature measurement techniques including seismic vibrations, electrical methods and ground temperature sensing. Geophysical profiles and maps were generated and used to identify permafrost features such as ice-rich and ice-poor zones. The study found that seismic shear wave velocity is influenced by ice content and can distinguish the active layer and permafrost layer. The research results regarding permafrost thickness reveal the impact of civil infrastructure, finding that buildings and roads can cause permafrost to degrade.

1 Introduction

Permafrost is soil with ground temperatures below 0 °C for at least two consecutive years. It is distributed across approximately 25% of the land surface in the northern hemisphere and is highly sensitive to atmospheric temperature variation primarily caused by global warming (Biskaborn et al., 2019; Lantuit et al., 2012). The Arctic annual surface temperature has increased by 3.1 °C from 1971 to 2019, which is three times faster than the global rate (AMAP, 2021; IPCC, 2021; Rantanen et al., 2022). In Utqiaġvik Alaska (study area), the average annual air temperature has risen over 4 °C since 1980, and recent decades have seen Arctic Alaska's permafrost warm by 1-3 °C (Thoman & Walsh, 2019; Nicolsky et al., 2017). Increasing temperature in the high-latitude permafrost regions leads to permafrost degradation, which includes permafrost warming, active layer thickening, and thaw-related hazards such as the development of taliks, ground subsidence and thermokarst in low-lying areas, mass wasting on slopes, and thermal erosion and abrasion along riverbanks and coasts (Hjort et al., 2022). Global warming causes contaminated and industrial sites in regions of stable permafrost to thaw, posing a significant environmental threat (Langer et al., 2023). Permafrost degradation drives serious changes in local geomorphology, hydrology, vegetation, wildlife dynamics, and greenhouse gas emissions (Streletskiy et al., 2015; Hjort et al., 2022).

Permafrost research often focuses primarily on ground temperature due to its direct effect on physical and biogeochemical soil processes, but permafrost is also affected by air temperature, snow cover, soil moisture, vegetation cover, and soil properties (Lantuit et al., 2012; Smith et al., 2022). In-situ monitoring using thermistors and thermocouples has shown that permafrost temperatures are increasing, leading to thawing and degradation (Nicolsky et al., 2009; Romanovsky et al., 2010; Shiklomanov et al., 2010; Nicolsky et al., 2017; Biskaborn et al., 2019). Understanding the ground's thermal state in permafrost regions is crucial to model and mitigate climate change impacts.

Understanding the spatial heterogeneity of permafrost in Arctic tundra is important for studying geomorphological and ecosystem variations under climate change, as well as potential engineering impacts. Permafrost structure is often complex due to fine-scale spatial heterogeneity of properties such as temperature and ice content. Temperature, saturation, and ice content influence seismic wave velocities, including shear wave velocity (V_s) and compressional wave velocity (V_p) (Coduto, 1999; Hjort et al., 2022; Ji et al., 2023; Liew et al., 2022; Rocha dos Santos et al., 2022). Here we provide an overview of some of the key permafrost structures investigated in this paper, including the active layer, cryopegs, ice-rich zones (e.g. lenses), and thermokarst lakes. Jafarov et al. (2016) showed that the active layer thickness (ALT) of undisturbed tundra near Elson Lagoon in Utqiaġvik, Alaska is approximately 0.2 to 0.6 m, measured in August 2013. A thermokarst is formed when the thermal equilibrium shifts, allowing the ground ice to thaw. Talik is a layer or body of year-round unfrozen ground (usually above 0 °C) occurring in a permafrost zone due to a local anomaly in thermal, hydrological, or hydrochemical conditions, e.g. underneath thermokarst lakes and rivers. Cryopegs are saline taliks that develop over time in shallow permafrost. As the climate warms, the annual ground temperature increases, annual thawing deepens until a certain threshold is met, after which a talik starts to develop. Ice wedges form when water seeps into cracks in the ground during summer and then freezes during winter. The distribution of ice formations and ice content within the permafrost layer is highly variable (Liu et al., 2021). In the coastal lowlands of Alaska's North Slope Borough, permafrost volumetric ice content is highly variable, with an average of ~80% (Kanevskiy et al., 2013). This results in a landscape vulnerable to widespread subsidence and thermokarst development, the magnitude of which may vary widely depending on surficial geology, ground ice volume, and the extent of past thermokarst activity (Farquharson et al., 2016). The warming and thawing of ice-rich permafrost pose changes in its interactions within the built environment (Hjort et al., 2022).

Permafrost exhibits vastly variable properties between thawed and frozen states due to the phase change of water, impacting its strength and bearing capacity, which can lead to infrastructure failure (Hjort et al., 2022). The interaction between permafrost and civil infrastructure contributes to permafrost degradation and increased construction and maintenance costs (Streletskiy et al., 2012, 2015). While existing research primarily focuses on the influence of degrading permafrost on infrastructure, it is crucial to consider the impact of civil infrastructure on permafrost. Different foundations and architecture, such as pile foundations and gravel roads, introduce thermal and physical impacts that can disturb the natural environment and alter adjacent tundra ecosystems (Walker et al., 2022). As climate change continues, the vulnerability of both civil infrastructure and permafrost systems grows, necessitating detailed knowledge of risk exposure in current and future infrastructure areas (Melvin et al., 2017; Hjort et al., 2022). Understanding the influence of civil infrastructure on degrading permafrost allows for a realistic risk assessment.

1.2 Seismic Imaging in Permafrost Regions

Seismic imaging is a commonly used technique for characterizing the subsurface in permafrost regions (e.g., Justice & Zuba, 1986; Miller et al., 2000; Ramachandran et al., 2011), because seismic wave velocities, including shear wave velocity and compressional wave velocity, are sensitive to temperature, saturation, and ice content (Coduto, 1999; Hjort et al., 2022; Liew et al., 2022; Ji et al., 2023). One of the main advantages of seismic imaging in permafrost regions is its ability to provide detailed information about the distribution and continuity of permafrost and the nature of the underlying soils, even 3D profiles with high resolution (e.g. Schwamborn et al., 2002; Ramachandran et al., 2011). This information is important for various applications, such as infrastructure planning and design, resource exploration, and environmental monitoring. Seismic refraction is a surface geophysics method that utilizes the refraction of body waves through layered media (Scott et al., 1990). Seismic refraction has been used in several case studies of permafrost conditions and periglacial environments (Harris & Cook, 1986; Ikeda, 2006; Schrott & Hoffmann, 2008). Joint inversion of refraction seismic tomography (RST) and electrical resistivity tomography (ERT) has been used to characterize Alpine rock glaciers and permafrost (Dou & Ajo-Franklin, 2014; Hubbard et al., 2013; Merz et al., 2015; Wagner et al., 2019). Brothers et al. (2016) previously used seismic reflection data to delineate continuous subsea ice-bearing permafrost.

Surface wave methods are powerful tools for near-surface characterization of sites and mapping irregular V_s profiles in permafrost through acquisition, processing, and inversion of surface waves, typically Rayleigh waves (Alam & Jaiswal, 2017; Carr et al., 1998; Essien et al., 2014; Fortin et al., 2007; Letson et al., 2019; Socco & Strobbia, 2004; Taylor et al., 2022). Compared with seismic refraction and reflection, surface wave methods are advantageous for mapping permafrost structures with low-velocity layers embedded under high-velocity layers (Dou & Ajo-Franklin, 2014). Spectral Analysis of Surface Waves (SASW) has been used to obtain S-wave velocity profiles of unfrozen and frozen soils in Fairbanks, Alaska (Hazirbaba et al., 2011; Cox et al., 2012). Multichannel Analysis of Surface Waves (MASW) has been applied in several permafrost studies, including to map deep low-velocity zones in coastal Arctic Alaska (Ajo-Franklin et al., 2017; Dou et al., 2012; Dou & Ajo-Franklin, 2014; Glazer et al., 2020; Majdański et al., 2022; Picotti et al., 2015; Rossi et al., 2018; Tourei et al., 2022). MASW has been combined with other technologies in permafrost research, such as seismic tomography and ERT (Marciniak et al., 2018; Marciniak et al., 2019; Glazer et al., 2020).

In this study, we investigate the spatial variability of permafrost in Utqiaġvik, Alaska, using MASW and ERT techniques to characterize permafrost, identify cryostructure, and analyze the influence of temperature on tundra permafrost systems. The MASW results provide useful information to verify ERT results for subsurface features. We compare in-situ temperature profiles with seismic velocity profiles to better understand the ground condition of the permafrost. This study is carried out across sites in undisturbed tundra and near infrastructure.

Our findings underscore the impact of civil infrastructure on permafrost degradation, particularly in designing and maintaining buildings in permafrost regions.

2 Study Area and Data Acquisition

2.1 Geologic Background

Permafrost zones underlie 80% of Alaska, including 29% continuous permafrost (Jorgenson et al., 2008). The North Slope Borough is entirely within the continuous permafrost zone (Ferrians, 1965; Kerkering, 2008), shown in Figure 1a. The permafrost in Utqiaġvik, Alaska, is continuous and has a thickness of approximately 200–400 m (Jorgenson et al., 2008). Elson Lagoon forms the eastern land boundary of the study area, shown in Figure 1b. The ALT of undisturbed tundra near Elson Lagoon is approximately 0.2 to 0.6 m, and the soil volumetric water content varies from 17% to 88%, measured in August 2013 (Jafarov et al., 2016). The ALT of the study area on the tundra in Utqiaġvik, Alaska, is less than 1.0 meter, consisting of three distinct layers: the acrotelm (top), the catotelm (middle), and the mineral soil (bottom) (Chen et al., 2020). The ground conditions vary from dry to marshy, with surface vegetation. The seismic survey (MASW) operations were performed on August 6 – 12, 2022. The plan layout of seismic survey lines and temperature measurement locations is shown in Figure 1.

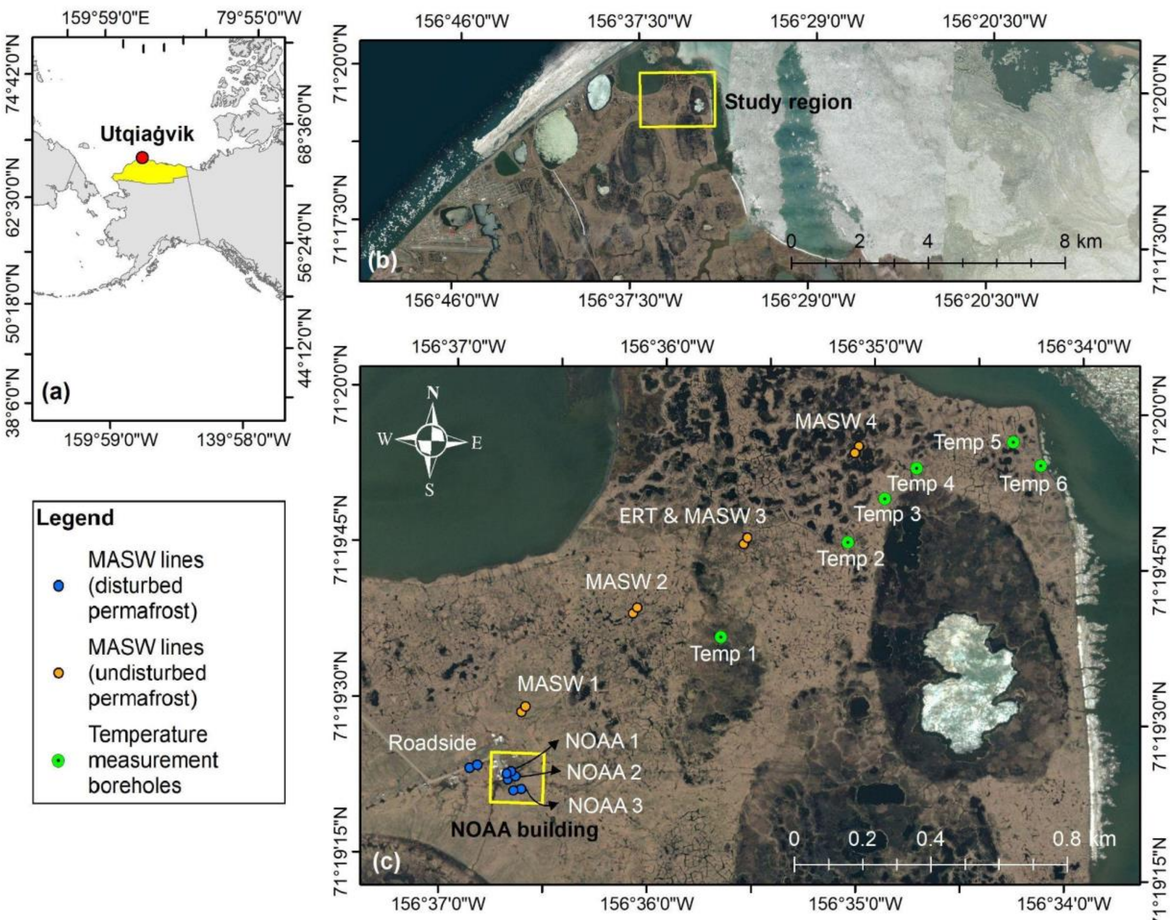

Figure 1. Seismic surveys (MASW) and temperature measurement map: (a) Utqiaġvik, North Slope Borough, Alaska. (b) Study region. (c) Seismic survey, electrical resistivity survey, and temperature measurement locations.

There are eight seismic survey locations using MASW, six temperature measurement locations using thermistors, one ERT survey location (at MASW 3 location), and five core sampling locations using hand-held drills (at Roadside and MASW 1-4 locations), as shown in Figure 1. The coordinates of these locations are provided in Table S1 in the Supporting Information. The seismic surveys cover various soil conditions, including disturbed and undisturbed areas, with and without infrastructure, and with medium to high water content. Four seismic surveys were performed on undisturbed tundra permafrost (without infrastructure development) and four on disturbed permafrost (with infrastructure development), shown in Figure 1c. The seismic surveys performed on disturbed permafrost include one survey along the gravel road near the National Oceanic and Atmospheric Administration (NOAA) facility (Roadside), one survey under the NOAA building (NOAA 1), one survey on the pre-existing building foundation next to the NOAA building (NOAA 2), and one survey on the tundra near the pile foundations (NOAA 3). At the NOAA 2 location, a building was demolished and removed one year prior to the seismic survey, but the pile foundations remain in the ground. The core sampling was performed at approximately 1 m from the seismic survey locations using a hand-held sampling drill. The sampling depth is up to 1.5 m.

2.2 Surface Wave Data Acquisition

Each seismic line consists of 24 vertical 4.5 Hz geophones (a 24-channel Geometrics Geode seismograph) positioned on the ground surface. Straight-line seismic profiles have geophone spacing equal to 1 m, which gives us a 23 m spread in total. We generated seismic signals using a sledgehammer adjacent to the geophones as well as an extra shot at 5 m offset from the beginning of the lines. The seismic record length was 128 ms with a sample interval of 0.25 ms, and each recording was initiated by a trigger attached to the sledgehammer. No pre-acquisition filter was used on the seismic data. Note that with the vertical source and the vertical receivers, the type of surface waves we acquired are Rayleigh waves. An example of the collected seismic traces is shown in Figure 2a.

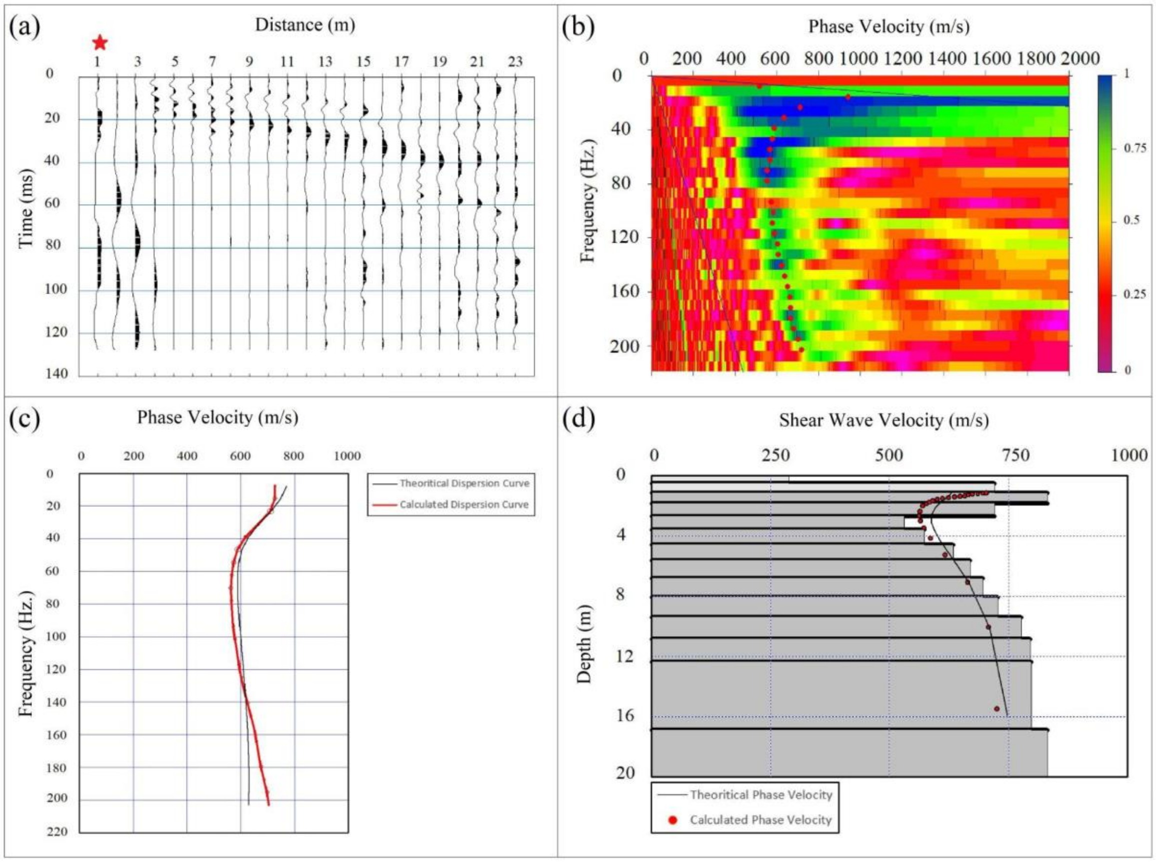

Figure 2. The procedure of building V_s models from extracted dispersion curve using MASW method: (a) The pre-processed shot-gather (Red star represents the shot location), (b) The calculated dispersion image representing Rayleigh wave phase velocity in each frequency (Red dots represent picks at high amplitudes), (c) The extracted dispersion curve from the dispersion image, and (d) V_s model inverted from the dispersion data.

2.3 Temperature Data Acquisition

Small 0.02-m diameter holes were punched in the ground to a depth of 1.5 meters in August 2021. Four HOBO TMC6-HD temperature sensors were then lowered into the ground using wooden rods to the depth of 0.02, 0.2, 0.5, and 1.5 m below the surface. At each location, temperature sensors were connected to two 2-channel HOBO U23-003 loggers in September 2022 (Supporting information). The operating temperature range for loggers is -40 to 100 ℃ with an accuracy of 0.4 ℃ and 0.2 ℃ below and above 0 ℃, respectively. The resolution is 0.02 ℃. Data records were collected during the field trip in August 2022. Because most of the commonly used construction materials are prohibited in this study area, reducing the vulnerability of the sensor installation to damages by wildlife animals is a challenging task and several temperature sensor cables were severed by Arctic foxes. Nevertheless, temperature records were collected at the six following sites. Site conditions were described during installation as follows. The Temp 1 profiler was placed into a shallow pond with 10 cm of standing water; The Temp 2 profiler is located near a rim of the flat-center ice-wedge polygon;

the site conditions could be described as moist. The Temp 3 station is placed at the center of a high-center polygon with a dry ground surface. The Temp 4 site is almost wet, with a thin layer of standing water in the middle of the low-center polygon. The Temp 5 profiler is at the rim of the low-center polygon, with the dry ground around it. Finally, the Temp 6 profiler is approximately 9 m from shore, where the ground is rather moist.

2.4 Electrical Resistivity Tomography Data Acquisition

An Electrical Resistivity Tomography (ERT) survey was conducted to provide in-situ resistivity measurements (Ωm) along the MASW 3 transect from September 13, 2022. The ERT station Syscal-Pro 72 (IRIS instruments) and steel electrodes were used to acquire data. Electrodes were placed along the transect using measuring tape with a 0.5 m spacing. Inverse Wenner-Schlumberger (WS) and Dipole-Dipole (DD) arrays were applied for measurements. The minimum/maximum half electrode spacing was 0.75m/17.25m for WS and 0.5m/13.5 m for the DD array. A 50 V output voltage and 250 ms pulse duration were applied during the survey. Contact resistances for most of the electrodes were no more than 1 kΩ. Measurements with errors exceeding 2% were removed during processing.

3 Imaging Methodology

3.1 Seismic Imaging Method

Surface waves can be generated by an active source, such as a hammer, weight drop, vibroseis, or by a passively recorded source, such as anthropogenic, traffic, or a number of other environmental sources (e.g. ocean waves, wind), and these waves are recorded by an array of geophones. Because surface waves can provide information on the subsurface velocities over a wide range of frequencies and wavelengths, the MASW technique can generate high-quality velocity models. MASW is often used to produce 1D velocity profiles, it can also be used to assess the lateral variability of the subsurface shear wave velocities, which is essential for characterizing subsurface heterogeneity and identifying areas of potential geotechnical concern. The MASW method can be applied in a wide range of geological environments and has the advantages of being non-invasive, cost-effective, and capable of providing high-resolution V_s profiles to depths of up to several tens of meters.

In active-source surface seismic surveys, over two-thirds of the total seismic energy generated by compressional waves is transmitted to Rayleigh waves, sometimes referred to as “ground roll” (Park et al., 1999b). An example of surface waves in our collected data is shown in Figure 2a. Surface wave energy decays exponentially with depth beneath the surface. Longer wavelength (i.e., longer-period and lower-frequency) surface waves travel deeper, thus containing more information about deeper velocity profiles. Shorter wavelength (i.e., shorter-period and higher-frequency) surface waves travel shallower, thus containing more information about shallower velocity profile. Surface waves are dispersive, meaning each wavelength propagates at different phase velocities in a layered medium. Thus, we can analyze phase velocity of different frequency bands (corresponding to different wavelengths) and estimate the velocity profile of the subsurface.

Rayleigh wave dispersion curves describe the velocity at which each wavelength travels. To determine Rayleigh wave dispersion curves, we use the phase shift method, which provides accurate fundamental-mode phase velocities even when only four geophones are used (Park et al., 1999b, Dal Moro et al., 2003). Our detailed procedure is provided in Supporting Information.

Figure 2 represents an example of the inversion procedure for estimating a 1D velocity profile. First, we applied a 7.50 - 327.68 Hz bandpass filter to all traces in a shot gather to remove high-frequency noise, and we muted noisy traces (Figure 2a). Then, we calculated dispersion images, determined phase velocities from picking the velocity with the maximum amplitude at each frequency (Figure 2b), and extracted the fundamental mode of Rayleigh surface wave from the dispersion image (Figure 2c). After wavelength-depth conversion, we generated an initial model based on the phase velocity picks. Finally, a non-linear least squares method (Xia et al., 1999) was applied to the dispersion curve to reconstruct the V_s velocity model (Figure 2d). Acceptable 1D models should have a root mean square (RMS) error of the difference between the theoretical dispersion and measured dispersion curves (Figure 2c) below 5% (SeisImagerSW^{TM} Manual, 2009). For 2D V_s estimation, we carry out the same pre-processing, then we perform dispersion analysis using the common mid-point (CMP) cross-correlation gathers.

Instead of common shot gather dispersion analysis, the CMP cross-correlation method of Hayashi & Suzuki (2004) increases the signal-to-noise ratio of the dispersion spectrum. The following steps are performed to conduct CMP cross-correlation analysis: First, we calculate cross-correlations between every pair of traces in each shot gather. Second, in the time domain, we collect correlation traces with a CMP and stack those with the same spacing. The resultant cross-correlation gathers resemble shot gathers and are known as CMP cross-correlation gathers. Third, we apply a multi-channel analysis to the CMP cross-correlation gathers to calculate the dispersion spectrum of surface waves. Finally, we invert the dispersion curve for each CMP to V_s model. As a general guideline, acceptable 2D models should result in an RMS below 15% (SeisImagerSW^{TM} Manual, 2009).

MASW is limited to shallow depth investigations, typically up to 30 meters. Beyond this depth, the resolution and accuracy of the method decrease significantly. Moreover, MASW is more suitable for homogeneous soil conditions and struggles to characterize layered or complex geological settings accurately. To overcome these limitations in the future, seismic refraction could be employed over a larger region as a complementary technique, although it will require more equipment than MASW. The depth and compression velocity information of different subsurface layers can be determined by analyzing the travel time data. Seismic refraction has the advantage of investigating deeper depths, making it useful for studying subsurface structures beyond the reach of MASW. The material in section S2 of the Supporting Information can serve as a basis for a future permafrost study combining MASW and seismic refraction. Advances in data acquisition and processing should be taken into account to ensure the best possible outcomes in future investigations. By integrating the strengths of these two techniques, it may be possible to enhance the accuracy and depth range of permafrost characterization.

3.2 Electrical Resistivity Tomography Imaging Method

Surface electrical resistivity surveying is based on the principle that the distribution of electrical potential in the ground around a current-carrying electrode depends on the electrical resistivities and distribution of the surrounding soils and rocks. The usual practice in the field is to apply an electrical direct current (DC) or alternating current (AC) of low frequency. True resistivity values of a media can be reconstructed through measured apparent resistivity values.

The voltage between two potential electrodes and the current between two other electrodes are measured during the ERT survey. Measurements were provided using various pairs of electrodes along the transect. An increase in spacing between electrodes allows for deeper investigation depth. Therefore, apparent resistivity values can be obtained through the voltage, current, and geometry of array electrodes for each point laterally and with depth. The apparent resistivity values must be inverted using data inversion programs to obtain true resistivity values of the subsurface materials.

Res2Dinv software (Res2Dinv Manual, 2006) was used to generate a resistivity model from apparent resistivity values. The inversion software uses a smoothness-constrained least squares method with L2-norm (Loke et al., 1996). We used robust constraint and defined an initial half-space resistivity value of 10 Ωm to trace spatial cryopegs distribution based on low resistivities observed in previous studies (Overduin et al., 2012; Yoshikawa et al., 2004; Hubbard et al., 2013). A 2D ERT model was generated to invert WS and DD arrays jointly, and the result achieved an RMS error of 1.8%.

ERT and other electromagnetic methods give us inherently non-unique solutions for mapped reconstructions of subsurface electrical properties. This non-uniqueness means that the measured data can be explained equally well by multiple models. To improve the reliability of subsurface interpretations, we use coring and comparison with other geophysical methods.

4 Results and Discussion

In the following sections, we provide an overview of the V_s, electrical resistivity, and temperature results. We highlight key results related to permafrost, including site characterization (4.1), shear wave velocity interpretation (4.2), civil infrastructure's influence on permafrost (4.3), and applications to engineering properties and infrastructure design (4.4).

4.1 Site characterization of disturbed and undisturbed permafrost

We calculated 1D and 2D V_s models for 8 survey lines after performing inversion on the calculated dispersion curves using the MASW method (Park et al., 1999a, 1999b). This included both disturbed and undisturbed permafrost regions. Figure 3 shows the 1D V_s profiles for the survey locations on the tundra, which are categorized as undisturbed permafrost locations. Figure 3a shows the V_s profile for the first location of MASW survey in the tundra (MASW 1), approximately 500 meters from the road and NOAA facility. The highest V_s is 978 m/s. A similar V_s profile is observed in Figures 4b-d unless the relative high-velocity zone is located relatively at a lower depth and has a more consistent velocity profile at higher depths than MASW 1. This could be an effect of the different geology, vegetation, or the effect of anthropogenic activities over the years, as we observed many marked points for previous studies and tracks from vehicles in the field. Figure 3b represents the V_s for the second location in the tundra (MASW 2), approximately 1 km from the infrastructure. We observe a very high-velocity zone at depth of 2-8 meters below the surface, representing an ice-rich zone. The highest V_s layers are located at 9 meters depth and are as high as 1700 m/s. This location clearly shows the undisturbed permafrost area with higher V_s and higher ice content. Figure 3c illustrates the velocity model for the third location in the tundra (MASW 3), which is located roughly 1.5 km from the road and NOAA building. While the low-high-low V_s pattern is obvious, the highest velocity is 1575 m/s, which is lower than that at the MASW 2 at 1 km. In the field, we observed that as we get further to the tundra, the ground gets wetter as indicated by many ponds in the area. This can also be seen on satellite map in Figure 8c-d (presented later in this paper), where the last two lines (MASW 3 and 4) are located in darker areas that represent higher surface water content. Figure 3d illustrates the velocity model for the last location in the tundra (MASW 4) at roughly 2 km distance from the road and NOAA building. Like all other locations in the tundra, we observed the low-high-low velocity profile, but the highest velocity zone is located at deeper depths of 7 meters. In addition, the highest V_s is 1150 m/s at MASW 4, which is lower than those at the two previous locations in undisturbed permafrost zones (MASW 2 and 3). These last two locations (MASW 3 and 4) represent the effect of vegetation and high surface water content. The previously observed low-high-low velocity profile below the surface by Dou & Ajo-Franklin (2014) is captured at all tundra locations (i.e., MASW 1-4 and NOAA 3).

Figures 4e-g show the 1D V_s profiles for the survey locations near the NOAA building, including the roadside, within 1.0 meter of the NOAA building (NOAA 1), and ~80 meters away from the NOAA building (NOAA 3), where we expect high disturbance in permafrost. These locations are categorized as disturbed permafrost locations. The V_s at disturbed permafrost locations is lower than that at undisturbed permafrost locations, as the vegetation thus albedo are affected by human activities, and the ice content is lower than that in the undisturbed permafrost region. Figure 3e represents the V_s for the location within 1.0 meter of the gravel road leading to the NOAA facility, where we expect high disturbance in permafrost. The 1D velocity profile represents a low-high-low velocity pattern with the highest V_s of 850 m/s. It is noted that the data at the pre-existing demolished building foundation next to the NOAA building (NOAA 2) are low-quality, which resulted in higher RMS error than the acceptable error. As we performed sledgehammer shots on top of a pre-existing building foundation, the contrast in soil and pile material properties and the resulting scattered energy likely generated relatively larger errors than in other locations.

Figure 4 shows the 2D V_s models in the undisturbed (5a-d) and disturbed (5e-g) permafrost regions similar to Figure 3. A low-high-low velocity pattern is evident in all models, indicating active layer (with low velocity), ice-rich permafrost (with high velocity), and partially frozen permafrost (low velocity). Previous studies have shown a strong correlation between permafrost temperature and V_s (Nakano et al., 1972; Kurfurst, 1976; Ji et al., 2023). The low-high-low velocity pattern is consistent with the general trend of permafrost temperature variation with depths, as in a previous study (Smith et al., 2022). Although the velocity and depth vary spatially, the low-high-low pattern is consistent among all locations. The 2D models capture the spatial variability of permafrost, demonstrating the importance of multichannel seismic surveys and 2D modeling. We will discuss these models in detail in sections 4.2 and 4.3.

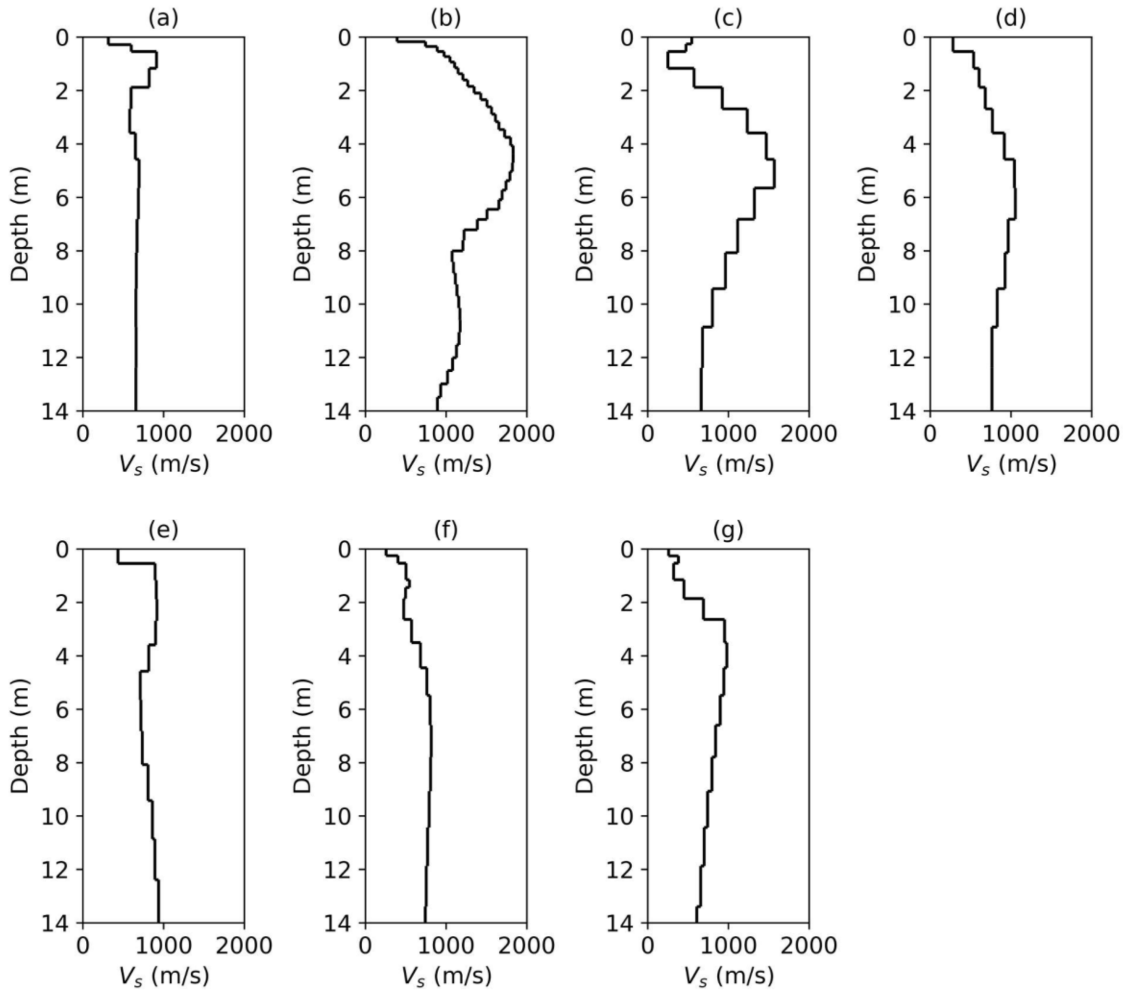

Figure 3. 1D V_s profiles for undisturbed (a-d) and disturbed (e-g) permafrost locations: (a) MASW 1, (b) MASW 2, (c) MASW 3, (d) MASW 4, (e) Roadside, (f) NOAA 1, and (g) NOAA 3.

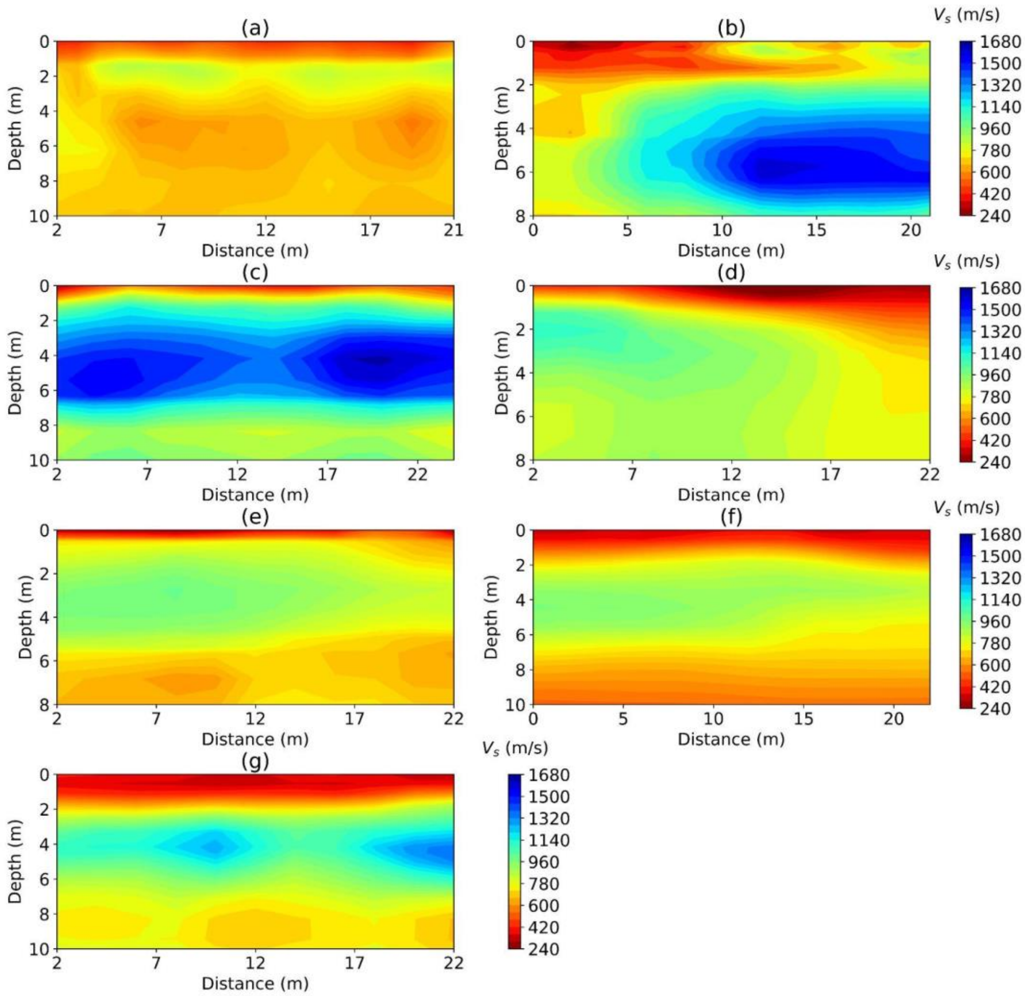

Figure 4. 2D V_s profiles for undisturbed (a-d) and disturbed (e-g) permafrost locations: (a) MASW 1, (b) MASW 2, (c) MASW 3, (d) MASW 4, (e) Roadside, (f) NOAA 1, and (g) NOAA 3.

Meanwhile, we invert the electrical resistivity model (in Figure 5a) from the ERT data, which can delineate several zones compared to the V_s model from the MASW 3 transect (Figure 5b). Each zone is characterized by different thicknesses, electrical resistivity, and velocity values. Zone A is characterized by relatively low resistivity up to 200-300 Ωm from the surface down to approximately 0.4 m. This layer represents the active layer and is characterized by low V_s of 240 m/s. Zone B is characterized by high resistivity values of 400-2000 Ωm. The thickness of this layer varies from 1 m at distances of 6-24 m to 4 m at distances 2-6 m. According to drilling data, the zone between 1.4 m and 1.7 m is a transition zone (black box marked in the borehole in Figure 5) between a frozen and unfrozen state and represents a boundary between zone B and C. Zone C is characterized by soils with low resistivity of 10-20 Ωm associated with cryopegs development in the study area. The thickness of the layer is about 2.5 m along the profile and decreases toward the beginning of the transect. Zone D is characterized by relatively high resistivity values of 100–600 Ωm and a thickness of about 2.5–3 m and is located between two zones of low resistivity (both zones denoted as Zone C). The zone is also characterized by high V_s up to 1600 m/s, which is typical for frozen material and increased ice content.

Due to the high contrast of the resistivity of different units, the ERT method helps to identify multiple layers in the upper part of the cross-section that cannot be clearly distinguished using the MASW method due to the lack of high-frequency signals. The MASW results provide useful information to verify ERT results at deeper depths.

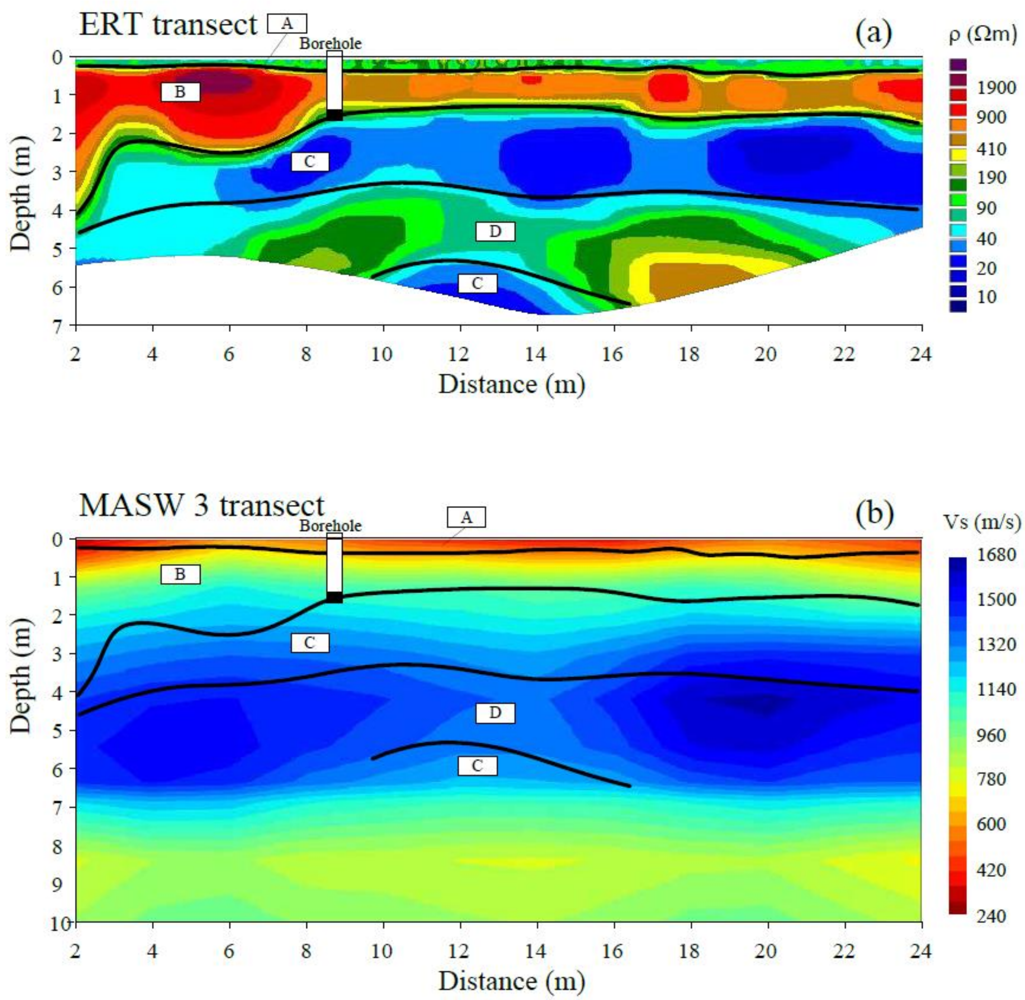

Figure 5. 2-D ERT (a) and MASW (b) comparison results at the MASW 3 location. Black lines represent interpreted ERT boundaries based on resistivity values.

4.2 Identification of active layer thickness

Significant variations in ALT exist between different landscape types, reflecting the influence of vegetation, substrate, microtopography, and especially soil moisture (Shiklomanov et al., 2010). Based on the boring samples collected at the same sites of the seismic surveys and nearby temperature measurements (described in Section 2.3 and shown in Figure 7 as Temp 1 - 6), ALT in the study region is 0.2 – 0.5 m.

From V_s profiles shown in Figure 4, we can identify the ALT range (roughly 0.3 m) and the shear wave velocities of the active layer (240 – 370 m/s) in most locations. However, in some undisturbed permafrost regions, ALT was found to be highly spatially heterogeneous due to differences in subsurface characteristics based on 2D V_s profiles shown in Figure 4. Therefore, ALT at some locations may be 0.5 – 0.6 m, which is consistent with the ALT range estimated from nearby temperature measurements (described in Section 2.3) and the earlier estimation by Jafarov et al. (2016). In contrast, ALT in disturbed permafrost regions presents higher values (0.5 – 1.0 m) and less spatial heterogeneity. The higher ALT indicates that the ground temperature is slightly higher for the permafrost with human activities than in the undisturbed permafrost. For NOAA 1 (Figure 3f), the high consistency in ALT is because the ground surface is under the NOAA facility and the topsoil is gravel, which is different from all other locations. The coverage of the building, which produces continuous heat, and the high thermal conductivity of gravel compared to fine-grained soil like peat or silt are likely contributing factors to the temperature consistency of the tested line. The MASW results did not reveal the top shallow active layer of MASW 3 due to the small ALT (0.22 m based on soil sampling) and lack of high-frequency source signal required to image shallow depths.

4.3 Identification of spatial heterogeneity of permafrost

Spatial heterogeneity within the permafrost layer can be observed and quantified by analyzing V_s profiles, including ice-rich permafrost, low-velocity zones, and talik. Shear wave velocities within the permafrost layer range from 450 to 1700 m/s. The shear wave velocities of ice-rich permafrost zones (MASW 2-4) are in the range of 700 – 1700 m/s, which is higher than the range of 500 – 900 m/s from other permafrost locations. Ice-rich permafrost can be identified in 2D V_s profiles, such as in Figure 4b (MASW 2), with a high-velocity zone (from 9 m to 22 m) with a V_s range of 1300 – 1700 m/s. The theoretical V_s of ice is approximately 1700 m/s at a temperature near -10 °C (Kohnen, 1974). This indicates that the center area of the ice-rich zone is likely composed primarily of ice layers. However, the gradual increase of the velocity near the ice-rich zone at MASW 2 indicates suspended soil around the ice layers.

Bodies of unfrozen material, taliks or cryopegs, can also be identified using V_s profiles. For example, a talik layer exists at MASW 3 at depth of 1.2 – 1.6 m with a corresponding V_s of 250 m/s. The boring log information shows that the soil is gray sandy silt with an ice lens gradually changing from frozen to unfrozen state from top to bottom at depth of 1.2 – 1.6 m, shown in Figure 6c. Figure 1c shows that MASW 3 is located in a wetter area (darker image color is related to higher surface water content), which may lead to open talik regions around the large water body. Another potential reason for this talik layer is salinity, as potentially higher salinity layers may exist at MASW 3 due to proximity of nearby saline thermokarst lake. The V_s range of the talik layer is similar to that of the active layer since the talik layer is unfrozen.

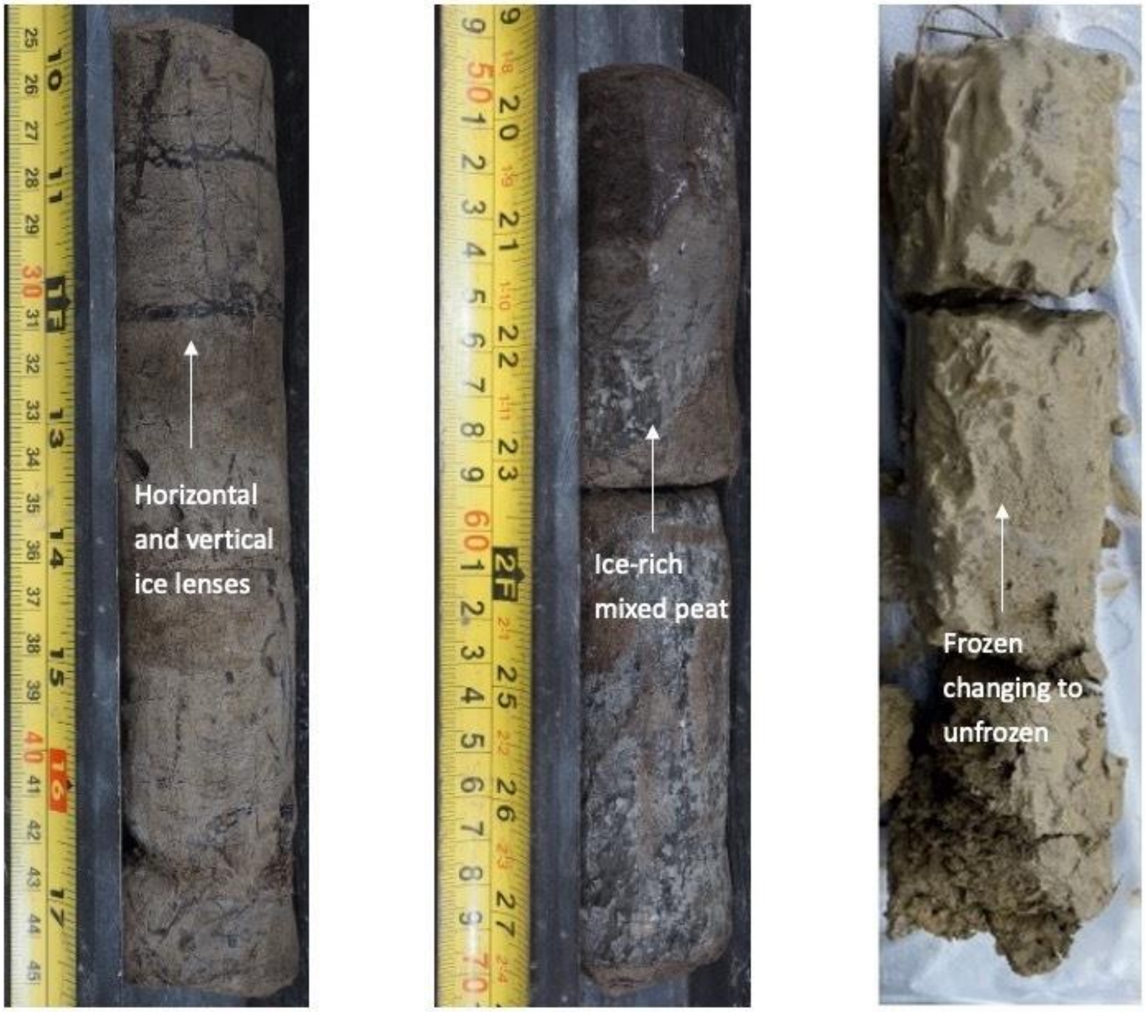

(a) Soil sample depth 0.22 – 0.46m
Silty peat to organic gray silt with ice lenses

(b) Soil sample depth 0.46 – 0.71 m
Ice-rich mixed peat and gray slightly organic silt

(c) Soil sample depth 1.42 – 1.68 m
Medium brown slightly sandy silt, from frozen (top) to unfrozen (bottom)

Figure 6. Permafrost samples at MASW 3.

Ice lenses cannot be directly recognized through V_s variations due to their small thickness at millimeter to centimeter scale. However, differences in V_s profiles between locations and depths can reflect variations in ice content. For example, at MASW 3, based on soil samples shown in Figures 7a and 7b, 1 – 3 mm thick ice lenses exist at the top of the permafrost layer (depth of 0.22 – 0.46 m), and then ice-rich permafrost presents at depth 0.46 – 1.42 m. The 1D V_s at MASW 3 (Figure 3c) reflects this transition from ice-poor to ice-rich permafrost as indicated by a high V_s layer at shallow depths. This suggests that the formation of ice lenses tends to develop during this transition. It is important to note that all V_s values are only representative of conditions in August 2022, and values may vary seasonally or over longer time scales.

4.4 Impacts of ground temperature and ice structure on shear wave velocities

In sections 4.4 and 4.5, we focus on the impacts of multiple factors on shear wave velocity in undisturbed permafrost to better understand permafrost behavior and stability. Figure 7 shows the composed profiles of V_s in undisturbed permafrost, temperature variation, and cryostratigraphy versus depth. The temperature difference between adjacent locations decreases with depth. The temperature measurements are derived from several locations near Utqiaġvik, Alaska. The detailed location and record date of the temperature measurement are presented in Figure S2 and Table S2 in the Supporting Information. The temperature reveals that the ALT is around 0.5 m, which agrees with the ALT determined from the MASW surveys.

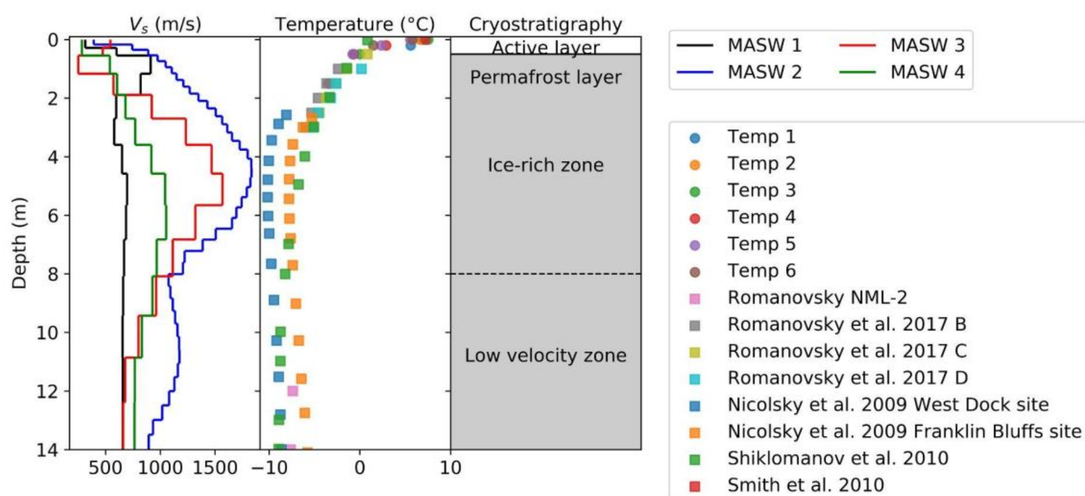

Figure 7. Composed velocity, temperature and stratigraphy profiles near Utqiaġvik, Alaska.

We observed that the depth variation of V_s exhibits a consistent trend across different testing locations near Utqiaġvik (see Figure 7). The V_s is low (~ 250 – 510 m/s) in the active layer and increases in the permafrost layer to around 1200 – 1700 m/s as depth increases to 5 – 8 m. Beyond this depth, the shear wave velocities decrease, forming a low-velocity permafrost zone (~500-700 m/s) beneath the high-velocity permafrost layer. The existence of a low-velocity permafrost zone was also reported by Dou and Ajo-Franklin's (2014) at a location approximately 20 km south of the study area. This suggests that low-velocity permafrost zones may exist under the tundra near Elson Lagoon and east of Utqiaġvik, Alaska. As shown in Figure 7, the V_s profiles are correlated with temperature profiles, with higher ground temperature corresponding to lower shear wave velocities of permafrost. The V_s values at each depth vary across locations for both the high and low-velocity zones, likely due to differences in ice content and ice layer formations.

Ice-wedge polygons occur on nearly all near-shore land surfaces (Kanevskiy et al., 2013) and can be outlined using 2D V_s profiles. The formation and degradation of these polygons are linked to climate change, resulting in severe landscape alteration. There are mainly three types of ice-wedge polygons in the tundra between Utqiaġvik and Elson Lagoon: high-centered polygons, flat-centered polygons (incipient polygons), and low-centered polygons. High-centered polygons are shown in Figure 8b, flat-centered polygons are shown in Figure 8c, and low-centered polygons are shown in Figure 8d, surrounded by thermokarst lakes. An early stage of high-centered polygon formation can be seen in Figure 8a, where V_s is lower due to lower moisture content compared with all other locations. Based on the satellite view between MASW 3 and 4, low-centered polygons (Figure 8d) develop and degrade from flat-centered and high-centered polygons, showing severe landscape alteration due to climate change along with lower V_s compared with high-centered polygon regions (Figure 8b). This transformation is referred to as ice-wedge polygon degradation. A water body in the center of the low-centered polygons can change the hydrological regime of polygon nets and lead to the onset of thermokarst activity (Kartoziia, 2019). As shown in Figure 8b, some of the high-centered polygons are developing and connecting, presenting ice-rich permafrost zones with high V_s, which have the potential to form thermokarst lakes during permafrost degradation. MASW 2 and 3 cover the polygon centers and troughs of high-centered polygons, while MASW 4 is on the rim between thermokarst lakes. For locations with surface water, V_s presents lower values on the top of the permafrost layer compared with adjacent permafrost.

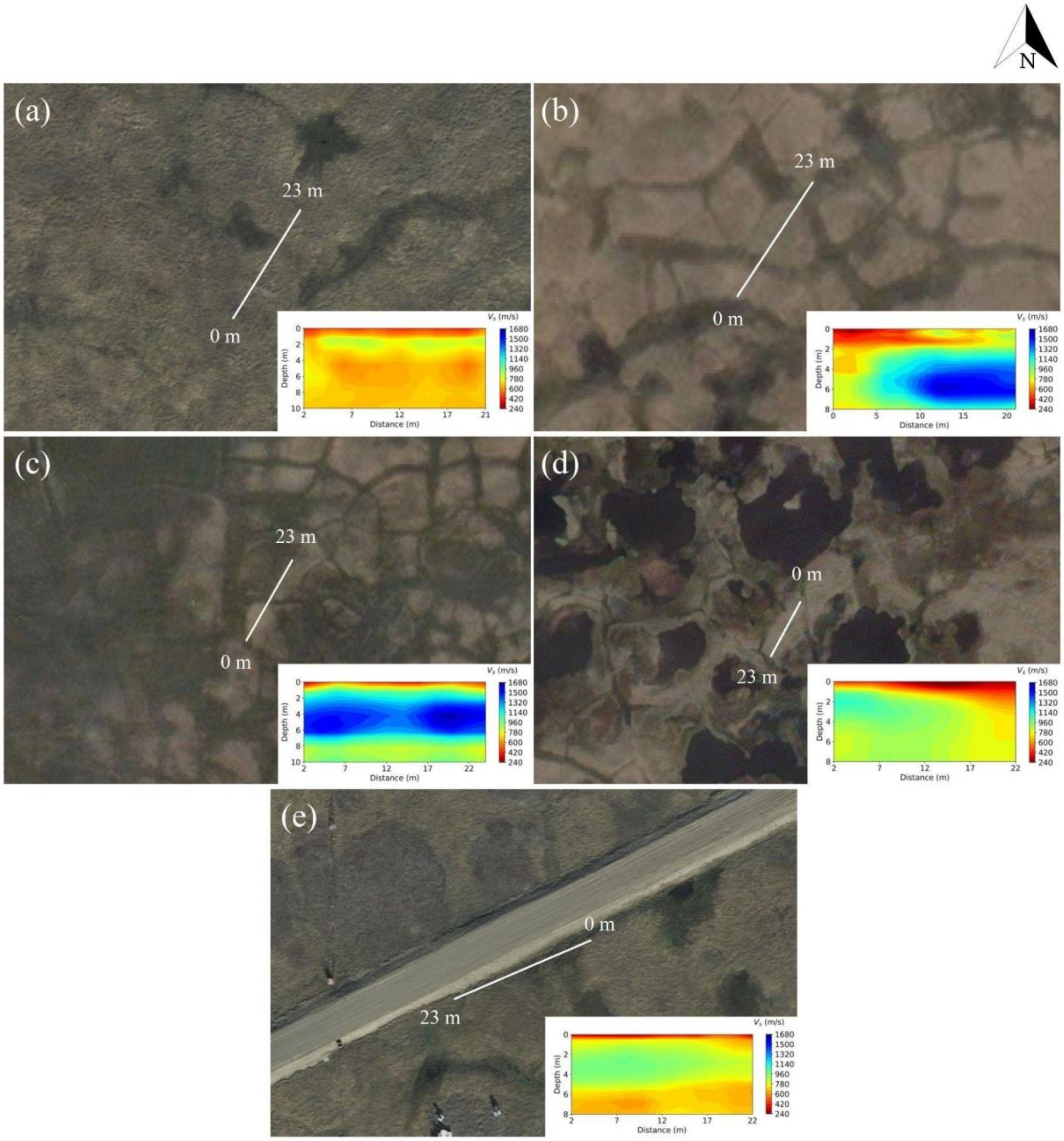

Figure 8. Satellite view of MASW testing locations in undisturbed permafrost tundra and disturbed permafrost roadside: (a) MASW 1, (b) MASW 2, (c) MASW 3, (d) MASW 4, and (e) Roadside.

4.5 Influence of civil infrastructure on permafrost

In this section, we discuss the influence of civil infrastructures, including a gravel road and pile foundations, two of the most common civil infrastructures in Northern Alaska, based on seven MASW surveys. Comparison of V_s profiles of disturbed permafrost locations (Roadside and NOAA 1) and relatively undisturbed permafrost locations nearby (NOAA 3 and MASW 1) in Figure 4 demonstrates that the ALT is larger in disturbed permafrost due to higher surface temperature. For NOAA 3 and MASW 1, the maximum V_s is similar (~900 m/s), but the high-velocity zone is deeper (~4 m) in permafrost near civil infrastructure (NOAA 1) compared with MASW 1 (~1 m). This discrepancy may be due to the disturbed gravel topsoil and also higher air temperatures near civil infrastructure, causing diffusive heat transfer from a more absorptive material and resulting in temperature profiles that differ from undisturbed permafrost locations.

The MASW testing location beside a gravel road is shown in Figure 8e (Roadside). In cold regions, dry coarse-grained soil is often used to replace the foundation soil of roadbeds or airport runways to prevent frost heave (Vinson et al., 1996). The gravel fill reduces the frost heave and thaw settlement of the road by providing better drainage capability but affects the moisture regime near the gravel road. As shown in Figure 8, high-centered polygons developed near the gravel road, with surface water accumulation next to the road embankment.

Ice-rich permafrost zones can be identified beneath the polygon landscape in the V_s profiles shown in Figures 5a and 9a. The depth of the ice-rich permafrost zone along the roadside (Figure 3e) is shallower than the nearby tundra location at NOAA 3 (Figure 3g), suggesting the influence of the gravel road. The ice-rich permafrost zone (~4 m thickness) along the roadside is thicker than MASW 1. Different moisture migrations beside the gravel road may cause these differences. In addition to unfrozen water migration as the dominant mode of moisture movement, vapor flux also contributes to frost heaving (Farouki, 1981; Currie, 1983; Smith & Burn, 1987; Teng et al., 2020). Gaseous water (vapor) migrates from the warm and humid side of the soil layer to the cold and dry layer below the closed and impermeable ground surface in coarse-grained soil and then condenses into ice, causing frost heaving (Guthrie et al., 2006; Niu et al., 2017; Zhang et al., 2020). This phenomenon is known as the “pot effect” or “canopy effect” (Bai et al., 2018). Generally, soil with an initial moisture content of less than 30% is more prone to showing the “pot effect” (Bai et al., 2018).

Pile foundations are the most common building foundation type in Arctic Alaska to overcome differential settlement. Figures 5f and 5g display the 2D V_s profiles for MASW surveys under the NOAA building (NOAA 1), and ~80 meters from the building in the tundra (NOAA 3), respectively. As shown in Figure 4, NOAA 1 shows a similar low-high-low V_s trend to NOAA 3 (and also MASW 1-4). At depths of 0-2 m, shear wave velocities are slightly different for NOAA 1 and NOAA 3 due to the topsoil of NOAA 1 being gravel, while NOAA 3 is tundra permafrost. At 2-8 m depths, NOAA 3 presents an ice-rich permafrost zone, while NOAA 1 has much smaller V_s in this depth range, indicating softer soil. In addition, in NOAA 1, we observed a ~150 m/s decrease in V_s for the ice-rich zone compared to the ice-rich zone at NOAA 3 (farther into the tundra). This lower V_s in the ice-rich zone near the building suggests that the pile foundation has an impact on the soil properties in the surrounding area. Although there is lower V_s in the ice-rich zone near the building, the ice-rich zone near the building is more laterally uniform than the ice-rich zone further in the tundra. Because the building had been present in the area for many years, it could have contributed to the thawing and freezing of the surrounding ground, leading to a more uniform distribution of ice-rich soil after years of thermal diffusion of heat from the building. The substantial differences observed at these sites highlight the need to consider the long-term effects of anthropogenic activities on the geological and geotechnical properties of the ground.

4.6 Applications in quantifying engineering properties and designing infrastructure on permafrost

Soil's mechanical properties can be determined using V_s, which is a commonly-used geotechnical and geophysical parameter. There are empirical or analytical correlations between V_s and several other soil properties. For instance, there is a positive correlation between V_s and soil stiffness parameters such as shear modulus (G) and elastic modulus (E). Stiffer soils generally exhibit higher shear wave velocities and are correlated with higher soil strength parameters such as undrained shear strength (S_u) and peak shear strength. In addition, V_s is inversely correlated with soil porosity, where lower V_s values are often observed in soils with higher porosity. V_s indicates soil density, as denser soils typically exhibit higher V_s values. Furthermore, soil classification, which determines the foundation design, directly correlates with V_{S30} and S_{u30}, which are the average of V_s and S_u in the top 30 meters (ASCE/SEI 7-16, 2017). Therefore, understanding the soil classification and V_s is crucial for assessing the seismic performance and stability of foundations and for designing appropriate foundation systems.

Investigating the long-term effect of civil infrastructure on permafrost's stiffness could help improve the engineering design of structures' foundations on permafrost. Therefore, we quantitatively analyze V_s profiles NOAA 1 and NOAA 3 locations. For soil that is elastic, isotropic, and homogeneous, the elastic theory can be used to establish the following relationship between elastic modulus and seismic wave velocity:

$$\mu = \frac{\left(\frac{V_p}{V_s}\right)^2 - 2}{2\left(\frac{V_p}{V_s}\right)^2 - 2}, \qquad (1)$$

$$G = \frac{\gamma V_s^2}{g}, \text{ and} \qquad (2)$$

$$E = 2G(1 + \mu), \qquad (3)$$

where, μ is the Poisson's ratio, G is the shear modulus, γ is the unit weight of the media, g is the gravitational acceleration, and E is elastic modulus, which can affect the foundation design in various ways such as foundation type, foundation settlement, and allowable vertical and lateral loads (Coduto, 1999). Based on the MASW results, V_{s30} for locations NOAA 1 and NOAA 3 are equal to 744.2 m/s and 799.5 m/s, respectively. Our lab tests have determined that the density of the permafrost core sample is 2000 kg/m3. Assuming a $V_p/V_s = 1.6$ for the site's permafrost layer based on (Ji et al., 2023), and g equals 9.81 m/s2, equations 1-3 result in an elastic modulus of 261.07 MPa at NOAA 1 location and 301.31 MPa at NOAA 3 location. This indicates a 13.35% reduction in elastic modulus.

5 Conclusions

This study uses 1D and 2D V_s profiles from MASW along with temperature measurement, ERT, and permafrost sampling to reveal various features of permafrost in Utqiaġvik, Alaska. V_s profiles can identify active layer, ice-rich permafrost, and talik in permafrost layer, but cannot identify cryostructures such as ice lenses due to their small scale. V_s in active layer ranges from 240 to 370 m/s (silty peat to silt), while V_s in permafrost layer ranges from 450 to 1700 m/s (silt to slightly sandy silt) in August 2022. V_s profiles demonstrate a consistent vertical low-high-low velocity trend in permafrost. Ice content, ice layers, and ice-wedge influence shear wave velocities, with higher V_s indicating higher ice content. Low V_s permafrost zones may exist across the tundra near Elson Lagoon and east of Utqiaġvik. The V_s variation in ice-rich permafrost correlates with ground temperature variation at depths of 0-15 m at the study site. This correlation indicates that ice-rich permafrost with higher V_s values demonstrates lower temperatures than active layer and ice-poor permafrost. By using ERT, multiple layers can be identified at shallow depths: active layer (200-300 Ωm), cryopeg (10-20 Ωm), and ice-rich permafrost (100-600 Ωm). The presence of ice becomes evident through the analysis of V_s and ERT profiles.

Civil infrastructure can impact permafrost, resulting in a higher active layer thickness and lower V_s. The influence of gravel road and pile foundation on permafrost degradation varies. Thicker ice-rich permafrost layers at shallower depths, surface water accumulation, and ice polygon development are identified near the grave road on permafrost. At the sites with building and pile foundation, lower shear wave velocities are observed at depths shallower than 7 m when compared to nearby undisturbed tundra. The active layer and permafrost are more laterally homogeneous closer to the building compared to nearby undisturbed tundra, and a thinner high-velocity zone exists closer to the building. The resulting V_s profile suggests weaker ground near infrastructure, which should be accounted for by civil engineers.

Acknowledgments

This study is supported by the National Science Foundation under Grants CMMI-2034363, CMMI-2034366, CMMI-2034380, and ICER-1927718. We express our gratitude to Geometrics for providing us with the necessary equipment and software for our study. We also acknowledge the support and facilities provided by UIC Science, LLC, the National Oceanic and Atmospheric Administration (NOAA), and the Atmospheric Radiation Measurement Climate Research Facility of the Department of Energy (DOE ARM). Dmitry Nicolsky acknowledges support from the Tomsk State University Development Programme (Priority-2030). We thank Dr. Min Liew for her valuable professional knowledge and advice, and Dr. Chris McComb for his assistance with fieldwork. Our sincere thanks also go to Larry Irons, an IT support at Colorado School of Mines, and Brian Passerella, equipment pool at Colorado School of Mines, for their invaluable assistance throughout the study.

Open Research

The seismic and ERT data have been submitted to The Arctic Data Center for open release and are currently under review prior to release and DOI assignment. Once these data have been released, this DOI will be added to the open data statement. Should any reviewers or editors wish to access this data submission as part of the review process, the authors would be happy to share a copy. The seismic data were processed using the SeisImagerSW software (Geometrics™), with parameters as described in Section 3.1. The ERT data were processed using the Res2Dinv software (Geotomo Software™), with parameters as described in Section 3.2. The physical permafrost samples photographed in Figure 6 have been submitted for registration through SESAR and are currently under review prior to release and IGSN assignment. The temperature data are available through The Arctic Data Center (Nicolsky & Wright, 2023).

References

Ajo-Franklin, J., Dou, S., Lindsey, N., Daley, T. M., Freifeld, B., Martin, E. R., Robertson, M., Ulrich, C., Wood, T., Eckblaw, I., & Wagner, A. (2017). Timelapse Surface Wave Monitoring of Permafrost Thaw Using Distributed Acoustic Sensing and a Permanent Automated Seismic Source. *SEG Technical Program Expanded Abstracts*, 5223–5227. https://doi.org/10.1190/SEGAM2017-17774027.1

Alam, M. I., & Jaiswal, P. (2017). Near Surface Characterization Using VP/VS and Poisson's Ratio from Seismic Refractions. *Journal of Environmental and Engineering Geophysics*, 22(2), 101–109. https://doi.org/10.2113/JEEG22.2.101

AMAP, Arctic Climate Change Update (2021). Key Trends and Impacts. *Summary for Policy-Makers, Arctic Monitoring and Assessment Programme (AMAP), Tromsø, Norway, 16*.

ASCE. (2017). ASCE/SEI 7-16. *Minimum Design Loads for Buildings and Other Structures*. https://doi.org/10.1061/9780784414248

Bai, R., Lai, Y., Zhang, M., & Gao, J. (2018). Water-vapor-heat behavior in a freezing unsaturated coarse-grained soil with a closed top. *Cold Regions Science and Technology*, *155*, 120-126.

Bery, A. A., & Bery, A. A. (2013). High Resolution in Seismic Refraction Tomography for Environmental Study. *International Journal of Geosciences*, *4*(4), 792–796. https://doi.org/10.4236/IJG.2013.44073

Biskaborn, B. K., Smith, S. L., Noetzli, J., Matthes, H., Vieira, G., Streletskiy, D. A., … & Lantuit, H. (2019). Permafrost is warming at a global scale. *Nature Communications*, 10(1), 264.

Bohlen, T. (2002). Parallel 3-D Viscoelastic Finite-Difference Seismic Modelling. *Computers & Geosciences*, 28(8), 887–899.

Brothers, L. L., Herman, B. M., Hart, P. E., & Ruppel, C. D. (2016). Subsea ice-bearing permafrost on the US Beaufort Margin: 1. Minimum seaward extent defined from multichannel seismic reflection data. *Geochemistry, Geophysics, Geosystems*, *17*(11), 4354-4365.

Carr, B. J., Hajnal, Z., & Prugger, A. (1998). Shear-wave studies in glacial till. 1273–1284. *GEOPHYSICS, 63*(4), 1273-1284. https://doi.org/10.1190/1.1444429

Chen, J., Wu, Y., O'Connor, M., Cardenas, M. B., Schaefer, K., Michaelides, R., & Kling, G. (2020). Active layer freeze-thaw and water storage dynamics in permafrost environments inferred from InSAR. *Remote Sensing of Environment*, *248*, 112007.

Coduto, D. P. (1999). *Geotechnical Engineering Principles and Practices*. Prentice-Hall, Inc.

Cox, B. R., Wood, C. M., & Hazirbaba, K. (2012). Frozen and unfrozen shear wave velocity seismic site classification of Fairbanks, Alaska. *Journal of Cold Regions Engineering*, *26*(3), 118-145.

Currie, J. A. (1983). Gas diffusion through soil crumbs: the effects of wetting and swelling. *Journal of Soil Science*, *34*(2), 217-232.

Dal Moro, G., Pipan, M., Forte, E., & Finetti, I. (2003). Determination of rayleigh wave dispersion curves for near surface applications in unconsolidated sediments. *SEG Technical Program Expanded Abstracts, 22*(1), 1247–1250. https://doi.org/10.1190/1.1817508

Dou, S., & Ajo-Franklin, J. B. (2014). Full-wavefield inversion of surface waves for mapping embedded low-velocity zones in permafrost. *Geophysics*, *79*(6), EN107-EN124.

Dou, S., Ajo Franklin, J. B., & Dreger, D. S. (2012, December). Mapping Deep Low Velocity Zones in Alaskan Arctic Coastal Permafrost using Seismic Surface Waves. In *AGU Fall Meeting Abstracts* (Vol. 2012, pp. C22B-07).

Essien, U. E., Akankpo, A. O., & Igboekwe, M. U. (2014). Poisson's Ratio of Surface Soils and Shallow Sediments Determined from Seismic Compressional and Shear Wave Velocities. *International Journal of Geosciences, 5*(12), 1540–1546. https://doi.org/10.4236/IJG.2014.512125

Farouki, O. T. (1981). The thermal properties of soils in cold regions. *Cold Regions Science and Technology*, *5*(1), 67-75.

Farquharson, L. M., Romanovsky, V. E., Cable, W. L., Walker, D. A., Kokelj, S. V., & Nicolsky, D. (2019). Climate change drives widespread and rapid thermokarst development in very cold permafrost in the Canadian High Arctic. *Geophysical Research Letters, 46*(12), 6681–6689.

Ferrians Jr, O. J. (1965). *Permafrost map of Alaska* (No. 445).

Fortin, J., Guéguen, Y., & Schubnel, A. (2007). Effects of pore collapse and grain crushing on ultrasonic velocities and Vp/Vs. *Journal of Geophysical Research: Solid Earth, 112*(B8), 8207. https://doi.org/10.1029/2005JB004005

Glazer, M., Dobiński, W., Marciniak, A., Majdański, M., & Błaszczyk, M. (2020). Spatial distribution and controls of permafrost development in non-glacial Arctic catchment over the Holocene, Fuglebekken, SW Spitsbergen. *Geomorphology, 358*, 107128.

Guthrie, W. S., Hermansson, Å., & Woffinden, K. H. (2006). Saturation of granular base material due to water vapor flow during freezing: laboratory experimentation and numerical modeling. In *Current Practices in Cold Regions Engineering*(pp. 1-12).

Harris, C., & Cook, J. D. (1986). The detection of high altitude permafrost in Jotunheimen, Norway using seismic refraction techniques: an assessment. *Arctic and Alpine Research*, *18*(1), 19-26.

Hayashi, K., & Suzuki, H. (2004). CMP cross-correlation analysis of multi-channel surface-wave data. In *Exploration Geophysics (Vol. 35, Issue 1)*.

Hazirbaba, K., Zhang, Y., & Hulsey, J. L. (2011). Evaluation of temperature and freeze–thaw effects on excess pore pressure generation of fine-grained soils. *Soil dynamics and earthquake engineering*, *31*(3), 372-384.

Hjort, J., Streletskiy, D., Doré, G., Wu, Q., Bjella, K., & Luoto, M. (2022). Impacts of permafrost degradation on infrastructure. *Nature Reviews Earth & Environment*, *3*(1), 24-38.

Hubbard, S. S., Gangodagamage, C., Dafflon, B., Wainwright, H., Peterson, J., Gusmeroli, A., … & Ulrich, C. (2013). Quantifying and relating land-surface and subsurface variability in permafrost environments using LiDAR and surface geophysical datasets. *Hydrogeology Journal*, *21*, 149–169. https://doi.org/10.1007/s10040-012-0939-y

Ikeda, A. (2006). Combination of conventional geophysical methods for sounding the composition of rock glaciers in the Swiss Alps. *Permafrost and Periglacial Processes*, *17*(1), 35-48.

IPCC. (2021). *Climate Change 2021: The Physical Science Basis, Contribution of Working Group I to the Sixth Assessment Report of the Intergovernmental Panel on Climate Change*. Cambridge University Press.

Jafarov, E., Parsekian, A., Schaefer, K., Liu, L., Chen, A., Panda, S. K., & Zhang, T. (2018). Pre-ABoVE: Active Layer Thickness and Soil Water Content, Barrow, Alaska, 2013. ORNL DAAC, Oak Ridge, Tennessee, USA.

Ji, X., Xiao, M., Martin, E. R., & Zhu, T. (2023). Statistical Evaluation of Seismic Velocity Models of Permafrost. *Earth ArXiv*. *Preprint*. https://doi.org/10.31223/X55080

Jorgenson, M. T., Yoshikawa, K., Kanevskiy, M., Shur, Y., Romanovsky, V., Marchenko, S., … & Jones, B. (2008, June). Permafrost characteristics of Alaska. In *Proceedings of the ninth international conference on permafrost* (Vol. 3, pp. 121-122). University of Alaska.

Justice, J. H., & Zuba, C. (1986). Transition zone reflections and permafrost analysis. *Geophysics*, *51*(5), 1075-1086.

Kanevskiy, M., Shur, Y., Jorgenson, M. T., Ping, C. L., Michaelson, G. J., Fortier, D., … & Tumskoy, V. (2013). Ground ice in the upper permafrost of the Beaufort Sea coast of Alaska. *Cold Regions Science and Technology*, *85*, 56-70.

Kartoziia, A. (2019). Assessment of the ice wedge polygon current state by means of UAV imagery analysis (Samoylov Island, the Lena Delta). *Remote Sensing*, *11*(13), 1627.

Kerkering, J. (2008). Mapping past and future permafrost extent on the North Slope Borough, Alaska.

Kneisel, C., Hauck, C., Fortier, R., & Moorman, B. (2008). Advances in geophysical methods for permafrost investigations. *Permafrost and Periglacial Processes*, *19*(2), 157–178. https://doi.org/10.1002/PPP.616

Kohnen, H. (1974). The temperature dependence of seismic waves in ice. *Journal of Glaciology*, *13*(67), 144-147.

Kurfurst, P. J. (1976). Ultrasonic wave measurements on frozen soils at permafrost temperatures. *Canadian Journal of Earth Sciences*, *13*(11), 1571-1576. https://doi.org/10.1139/e76-163

Langer, M., von Deimling, T. S., Westermann, S., Rolph, R., Rutte, R., Antonova, S., … & Grosse, G. (2023). Thawing permafrost poses environmental threat to thousands of sites with legacy industrial contamination. *Nature Communications*, *14*(1), 1721. https://doi.org/10.1038/s41467-023-37276-4

Lantuit, H., Overduin, P. P., Couture, N., Wetterich, S., Aré, F., Atkinson, D., … & Vasiliev, A. (2012). The Arctic coastal dynamics database: A new classification scheme and statistics on Arctic permafrost coastlines. *Estuaries and Coasts*, *35*, 383-400.

Letson, F., Barthelmie, R. J., Hu, W., Brown, L. D., & Pryor, S. C. (2019). Wind gust quantification using seismic measurements. *Natural Hazards*, *99*(1), 355–377. https://doi.org/10.1007/S11069-019-03744-8/FIGURES/11

Liew, M., Ji, X., Xiao, M., Farquharson, L., Nicolsky, D., Romanovsky, V., ... & McComb, C. (2022). Synthesis of physical processes of permafrost degradation and geophysical and geomechanical properties of permafrost. *Cold Regions Science and Technology*, *198*, 103522.

Liu, H., Maghoul, P., & Shalaby, A. (2021). Seismic physics-based characterization of permafrost sites using surface waves. *Cryosphere Discussions*.

Loke, M. H., & Barker, R. D. (1996). Rapid least-squares inversion of apparent resistivity pseudosections by a quasi-Newton method. *Geophysical Prospect. 44*, 131–152.

Majdański, M., Dobiński, W., Marciniak, A., Owoc, B., Glazer, M., Osuch, M., & Wawrzyniak, T. (2022). Variations of permafrost under freezing and thawing conditions in the coastal catchment Fuglebekken (Hornsund, Spitsbergen, Svalbard). *Permafrost and Periglacial Processes*, *33*(3), 264–276. https://doi.org/10.1002/ppp.2147

Marciniak, A., Owoc, B., Grzyb, J., Glazer, M., Dobiński, W., & Majdański, M. (2018, April). Seismic Tomography and MASW analysis of the results of Spitsbergen seismic experiment-case study. In *EGU General Assembly Conference Abstracts* (p. 280).

Marciniak, A., Owoc, B., Wawrzyniak, T., Nawrot, A., Glazer, M., Osuch, M., ... & Majdański, M. (2019, September). Near-Surface Geophysical Imaging of the Permafrost—Initial Result of Two High Arctic Expeditions to Spitsbergen. In *25th European Meeting of Environmental and Engineering Geophysics* (Vol. 2019, No. 1, pp. 1-5). European Association of Geoscientists & Engineers.

Melvin, A. M., Larsen, P., Boehlert, B., Neumann, J. E., Chinowsky, P., Espinet, X., ... & Marchenko, S. S. (2017). Climate change damages to Alaska public infrastructure and the economics of proactive adaptation. *Proceedings of the National Academy of Sciences*, *114*(2), E122-E131.

Merz, K., Maurer, H., Buchli, T., Horstmeyer, H., Green, A. G., & Springman, S. M. (2015). Evaluation of ground-based and helicopter ground-penetrating radar data acquired across an Alpine rock glacier. *Permafrost and Periglacial Processes*, *26*(1), 13-27.

Miller, R. D., Laflen, D. R., Hunter, J. A., Burns, R. A., Good, R. L., Douma, M., ... & Carr, B. J. (2000, August). Imaging permafrost with shallow P-and S-wave reflection. In *SEG International Exposition and Annual Meeting* (pp. SEG-2000). SEG.

Nakano, Y., Martin III, R. J., & Smith, M. (1972). Ultrasonic velocities of the dilatation and shear waves in frozen soils. *Water Resources Research*, *8*(4), 1024-1030. https://doi.org/10.1029/WR008i004p01024

Nicolsky, D. J., Romanovsky, V. E., & Panteleev, G. G. (2009). Estimation of soil thermal properties using in-situ temperature measurements in the active layer and permafrost. *Cold Regions Science and Technology*, *55*(1), 120-129.

Nicolsky, D. J., Romanovsky, V. E., Panda, S. K., Marchenko, S. S., & Muskett, R. R. (2017). Applicability of the ecosystem type approach to model permafrost dynamics across the Alaska North Slope. *Journal of Geophysical Research: Earth Surface*, *122*(1), 50-75.

Nicolsky, D. J., & Wright, T. (2023). Understand and forecast long-term variations of in-situ geophysical and geomechanical characteristics of degrading permafrost in the Arctic - continuously observed ground temperatures, 2021-2022 .[Dataset]. Arctic Data Center. https://doi.org/10.18739/A2C53F305

Niu, F., Li, A., Luo, J., Lin, Z., Yin, G., Liu, M., ... & Liu, H. (2017). Soil moisture, ground temperatures, and deformation of a high-speed railway embankment in Northeast China. *Cold Regions Science and Technology*, *133*, 7-14.

Overduin, P. P., Westermann, S., Yoshikawa, K., Haberlau, T., Romanovsky, V., & Wetterich, S. (2012). Geoelectric observations of the degradation of nearshore submarine permafrost at Barrow (Alaskan Beaufort Sea). *J. Geophys. Res.*, *117*, F02004. https://doi.org/10.1029/2011JF002088

Park, C. B. (2011). Imaging dispersion of MASW data - Full vs. Selective offset scheme. *Journal of Environmental and Engineering Geophysics*, *16*(1). https://doi.org/10.2113/JEEG16.1.13

Park, C. B., Miller, R. D., & Xia, J. (1999a). Multimodal Analysis of High Frequency Surface Waves. In *Symposium on the Application of Geophysics to Engineering and Environmental Problems 1999* (pp. 115–121). Environment and Engineering Geophysical Society. https://doi.org/doi:10.4133/1.2922596

Park, C. B., Miller, R. D., & Xia, J. (1999b). Multichannel analysis of surface waves. *GEOPHYSICS*, *64*(3), 800–808. https://doi.org/10.1190/1.1444590

Park, C. B., Miller, R. D., Xia, J., & Survey, K. G. (1998). Imaging dispersion curves of surface waves on multi-channel record. *SEG Technical Program Expanded Abstracts*. Proceedings of the National Academy of Sciences, 114(2), pp.E122-E131.

Picotti, S., Vuan, A., Carcione, J. M., Horgan, H. J., & Anandakrishnan, S. (2015). Anisotropy and crystalline fabric of Whillans Ice Stream (West Antarctica) inferred from multicomponent seismic data. *Journal of Geophysical Research: Solid Earth*, *120*(6), 4237-4262.

Res2Dinv Manual (2006). Geoelectrical Imaging 2D and 3D. (Version 3.59.) [Software]. Geotomo Software™.

Ramachandran, K., Bellefleur, G., Brent, T., Riedel, M., & Dallimore, S. (2011). Imaging permafrost velocity structure using high resolution 3D seismic tomography. *Geophysics*, *76*(5), B187-B198.

Rantanen, M., Karpechko, A. Y., Lipponen, A., Nordling, K., Hyvärinen, O., Ruosteenoja, K., Vihma, T., & Laaksonen, A. (2022). The Arctic has warmed nearly four times faster than the globe since 1979. *Communications Earth & Environment*, *3*(1), 1-10.

Romanovsky, V. E., Drozdov, D. S., Oberman, N. G., Malkova, G. V., Kholodov, A. L., Marchenko, S. S., … & Vasiliev, A. A. (2010). Thermal state of permafrost in Russia. *Permafrost and Periglacial Processes*, *21*(2), 136-155.

Rossi, G., Accaino, F., Boaga, J., Petronio, L., Romeo, R., & Wheeler, W. (2018). Seismic survey on an open pingo system in Adventdalen Valley, Spitsbergen, Svalbard. *Near Surface Geophysics*, *16*(1), 89-103.

Rocha dos Santos, G., Czarny, R., Roth, N., Zhu, T., Tourei, A., Martin, E. R., Ji, X., Liew, M., Jensen, A. M., Nicolsky, D., & Xiao, M. (2022). Identification of Cryoseismic Events in Utqia\.{g}vik, Alaska Using Distributed Acoustic Sensing (DAS). *AGU Fall Meeting Abstracts*, *2022*, NS45B-0326.

Ryden, N., Park, C. B., Ulriksen, P., & Miller, R. D. (2004). Multimodal Approach to Seismic Pavement Testing. *Journal of Geotechnical and Geoenvironmental Engineering*, *130*(6). https://doi.org/10.1061/(asce)1090-0241(2004)130:6(636)

Schrott, L., & Hoffmann, T. (2008). Refraction seismics. *Applied Geophysics in periglacial environments*, 57-79.

Schwamborn, G. J., Dix, J. K., Bull, J. M., & Rachold, V. (2002). High-resolution seismic and ground penetrating radar–geophysical profiling of a thermokarst lake in the western Lena Delta, Northern Siberia. *Permafrost and Periglacial Processes*, *13*(4), 259-269.

Scott, J. H., & Markiewicz, R. D. (1990). Dips and Chips—PC Programs for Analyzing Seismic Refraction Data. In *Symposium on the Application of Geophysics to Engineering and Environmental Problems 1990* (pp. 175-200). Society of Exploration Geophysicists.

SeisImager/SW™ Manual (2009). SeisImager/SW™. (Version 3.0.) [Software]. Geometrics Inc.

Shiklomanov, N. I., Streletskiy, D. A., Nelson, F. E., Hollister, R. D., Romanovsky, V. E., Tweedie, C. E., ... & Brown, J. (2010). Decadal variations of active-layer thickness in moisture-controlled landscapes, Barrow, Alaska. *Journal of Geophysical Research: Biogeosciences*, *115*(G4).

Smith, M. W., & Burn, C. R. (1987). Outward flux of vapour from frozen soils at Mayo, Yukon, Canada: results and interpretation. *Cold Regions Science and Technology*, *13*(2), 143-152.

Smith, S. L., O'Neill, H. B., Isaksen, K., Noetzli, J., & Romanovsky, V. E. (2022). The changing thermal state of permafrost. *Nature Reviews Earth & Environment*, *3*(1), 10–23. https://doi.org/10.1038/s43017-021-00240-1

Socco, L. V., & Strobbia, C. (2004). Surface-wave method for near-surface characterization: A tutorial. *Near surface geophysics*, *2*(4), 165-185.

Streletskiy, D. A., Anisimov, O., & Vasiliev, A. (2015). Permafrost degradation. In *Snow and ice-related hazards, risks, and disasters* (pp. 303-344). Academic Press.

Streletskiy, D. A., Shiklomanov, N. I., & Nelson, F. E. (2012). Permafrost, infrastructure, and climate change: a GIS-based landscape approach to geotechnical modeling. *Arctic, Antarctic, and Alpine Research*, *44*(3), 368-380.

Taylor, O. D. S., Abdollahi, M., & Vahedifard, F. (2022). Statistical distributions of wave velocities and elastic moduli in near-surface unsaturated soils. *Soil Dynamics and Earthquake Engineering*, *157,* 107247.

Teng, J., Liu, J., Zhang, S., & Sheng, D. (2020). Modelling frost heave in unsaturated coarse-grained soils. *Acta Geotechnica*, *15,* 3307-3320.

Thoman, R., & Walsh, J. E. (2019). Alaska's changing environment: Documenting Alaska's physical and biological changes through observations. *International Arctic Research Center, University of Alaska Fairbanks*.

Tourei, A., Martin, E. R., Rocha dos Santos, G., Czarny, R., Roth, N., Zhu, T., Ji, X., Liew, M., Jensen, A. M., Nicolsky, D., & Xiao, M. (2022). Exploration and Quality Control of Large-scale Distributed Acoustic Sensing Data to Study Permafrost Degradation in Arctic Alaska. *AGU Fall Meeting Abstracts, 2022,* NS22B-0291.

Vinson, T. S., Rooney, J. W., & Haas, W. H. (Eds.). (1996). *Roads and airfields in cold regions: a state of the practice report*. ASCE Publications.

Wagner, F. M., Mollaret, C., Günther, T., Kemna, A., & Hauck, C. (2019). Quantitative imaging of water, ice and air in permafrost systems through petrophysical joint inversion of seismic refraction and electrical resistivity data. *Geophysical Journal International*, *219*(3), 1866-1875.

Walker, D. A., Raynolds, M. K., Kanevskiy, M. Z., Shur, Y. S., Romanovsky, V. E., Jones, B. M., ... & Peirce, J. L. (2022). Cumulative impacts of a gravel road and climate change in an ice-wedge-polygon landscape, Prudhoe Bay, Alaska. *Arctic Science*, *8*(4), 1040-1066.

Xia, J., Miller, R. D., & Park, C. B. (1999). Configuration of Near-Surface Shear-Wave Velocity by Inverting Surface Wave. In *Symposium on the Application of Geophysics to Engineering and Environmental Problems 1999* (pp. 95–104). Environment and Engineering Geophysical Society. https://doi.org/doi:10.4133/1.2922698

Yilmaz, O. (1987). Seismic deta processing. *Investigation in geophysics*, *2*, 526.

Yoshikawa, K., Romanovsky, V., Duxbury, N., Brown, J., & Tsapin, A. (2004). The use of geophysical methods to discriminate between brine layers and freshwater taliks in permafrost regions. *J. Glaciol. Geocryology 26*, 301–309.

Zhang, Y., Wen, A., Zhao, W., Liang, X., Li, P., & Černý, R. (2020). Influence of Compaction Level on the Water-Heat-Vapor Characteristics of Unsaturated Coarse-Grained Fillings Exposed to Freezing and Thawing. *Advances in Civil Engineering*, *2020*, 1-10.